The unique features in the four-day widespread extreme rainfall event over

North China in July 2023

Jinfang YIN[1,2,3], Feng LI[1], Mingxin LI[1], Rudi XIA[1], Xinghua BAO[1],

Jisong SUN[1], and Xudong LIANG[1]

[1] State Key Laboratory of Severe Weather, Chinese Academy of Meteorological

Sciences, Beijing 100081, China

[2] Research Center for Disastrous Weather over Hengduan Mountains & Low-Latitude

Plateau, China Meteorological Administration (CMA), Kunming 650034, China

[3] Shigatse National Climatological Observatory, CMA, Shigatse 857000, China

Submitted to *Natural Hazards and Earth System Sciences* (*NHESS*)

August 2024

Revised   November 2024

Corresponding author: Jinfang YIN

E-mail: yinjf@cma.gov.cn

ABSTRACT

Synoptic forcings have traditionally played a pivotal role in extreme rainfall over North China. However, there are still large unexplained gaps in understanding the formation of extreme rainfalls over this region. The heavy rainfall event, lasting from 29 July to 2 August 2023 (referred to as "23·7" event), is characterized by long duration, widespread coverage, and high accumulated rainfall over North China. Overall, the persistent extreme rainfall is closely associated with the remnant vortex originating from typhoon Doksuri(2305), tropical storm Khanun(2306), and the unusual westward extended western Pacific subtropical high (WPSH), as well as quasi-stationary cold dry air masses surrounding North China on the west and north sides. Based on wind profiles and rainfall characteristics, the life history of the "23·7" event is divided into two stages. In the first stage, the western boundary of the western Pacific subtropical high (WPSH) was destroyed by the tropical storm Doksuri, appearing that the WPSH retreated eastward with decreasing height. As a result, an inclined vertical distribution on the western boundary was established below 500 hPa. Therefore, convections were limited by the tilted WPSH with warm-dry cover embedded in the low-to-middle troposphere. Meanwhile, the orography in the west of North China was controlled by cold air masses above nearly 3.0 km. Combining the orographic and cold air blockings, only a shallow southeasterly layer (between 1.3 and 3.0 km) can overpass mountains. Although the warm and moist southeasterly flows were lifted by orography, no convections were triggered because of the local capped cold and dry air masses overhead. Under this framework, equivalent potential temperature (θ_e) gradients were established between warm humid and dry cold air masses, similar to a warm front, causing warm air to lift and generate widespread rainfall but low intensity. However, the lifting was too weak to allow convection to be highly organized. In the second stage, the WPSH was further destroyed by enhanced Khanun, and thus the embedded warm-dry cover associated with the tilted WPSH was significantly thinned. Consequently, convections triggered by orographic blocking can move upward and consequently further develop, forming deep convections. Comparatively speaking, the convections in the second stage are much deeper than those in the first stage. The results gained herein may shed new light on better understanding and forecasting of long-lasting extreme rainfall.

1. Introduction

A persistent severe rainfall event occurred over central and North China during the period from 29 July to 2 August 2023, which was regarded as one of the precipitation extremes of 2023 globally (Fowler et al., 2024). Despite the rainfall in low intensity, it was long-lasting and widespread, resulting in large accumulated rainfall. Flooding from this event affected 1.3 million people, bringing severe human casualties and economic losses. One of the distinct features of this rainfall event was closely associated with the remnant vortex originating from typhoon Doksuri(2305), tropical storm Khanun(2306), unusual westward extended western Pacific subtropical high (WPSH), and quasi-stationary cold dry air masses surrounding North China on the west and north sides.

It is common for rainfall occurrence over North China due to strong water vapor supply by tropical cyclones over the East China Sea and/or Southern China Sea (e.g., Ding,1978; Feng and Cheng,2002; Yin et al.,2022c). Like the "96·8" heavy rainfall event (Sun et al.,2006; Bao et al., 2024), the present persistent rainfall event was closely linked to two tropical storms of Doksuri and Khanun. Note that the Doksuri weakened to a typhoon remnant vortex (typhoon-low pressure) at this moment as it moved inland after landfalling, while the tropical storm Khanun was in a fast-developing stage. The tropical storm Khanun and the typhoon remnant vortex built a water vapor bridge, transporting a large amount of water vapor to North China from the East China Sea. Previous studies (e.g., Hirata and Kawamura,2014; Gao et al.,2022; Yang et al.,2017) pointed out that large amounts of water vapor brought by a typhoon over the North Pacific were favorable for heavy rainfall generation in eastern China.

In the last several decades, considerable attention was paid to the remote rainfall events associated with tropical cyclones, and substantial progress has been made (e.g., Wang et al., 2009; Xu et al.,2023a; Xu et al.,2023b; Lin and Wu,2021). Commonly, sufficient water vapor provided by a tropical cyclone plays an important role in extreme rainfall over North China (e.g., Rao et al.,2023; Xu et al.,2023b). Besides, many studies confirmed that the WPSH is closely related to water vapor transportation and the spatial distribution of rainfall (e.g., Hu et al.,2019; Gao et al.,2022). Additionally, orographic forcing of the approaching warm and moist unstable air plays a critical role in determining the location of convection initialization, although

删除的内容: such large-scale weather conditions were favorable for heavy rainfall generation

删除的内容: surface

82 sometimes orographic forcing played a small role compared to Typhoon's circulation (Wang et

83 al.,2009). Moreover, heavy rainfall can be generated by the complicated cloud microphysical

84 processes due to the interactions between tropical oceanic warm-moist and mid-latitude cold-

85 dry air masses (Wang et al.,2009; Xu and Li,2017; Xu et al.,2021). Despite some experiences

86 gained, there are still large unexplained gaps in understanding the formation of extreme rainfall

87 (Meng et al.,2019). In this event, no highly organized strong convective system was observed,

88 and rainfall was featured by long duration, widespread coverage, and high accumulation.

89 Although operational forecasts gave reasonable results at that time, several unusual features

90 were found to exist in this extreme rainfall event. Some unexplainable questions have been

91 raised after the persistent heavy rainfall event: (1) What mechanism(s) could account for the

92 persistent heavy rainfall? (2) What is the role of the unusual westward extended WPSH in

93 governing the rainfall over North China? Therefore, we are motivated to conduct the present

94 modeling study to answer those questions.

95 The rest of the paper is organized as follows. A detailed description of the main features

96 of extreme rainfall and synoptic-scale weather conditions is documented. Section 3 provides

97 detailed model configuration and verification against observations. We present a detailed

98 analysis of the extreme rainfall production in Section 4. The paper finishes with conclusions

99 and outlooks.

100 **2. Properties of rainfall and wind profiles**

101 *2.1 Characteristics of rainfall*

102 Figure 1 shows the spatial distribution of 96-h accumulated rainfall from observations

103 during the period from 0000 UTC 29 July to 0000 UTC 2 August 2023, with the peak amount

104 of 1004 mm at Liangjiazhuang station near Xingtai, Hebei Province of North China.

105 Exceptionally long duration of rainfall is a notable feature of the event, with the longest duration

106 being 80 hours within the four days at some stations. The spatial distribution of the rain belt

107 with three heavy rainfall cores is consistent with the orography of the Yanshan Mountains on

108 the north and the Taihang Mountains on the south, suggesting that orography plays an important

109 role in the precipitation. It should be emphasized that three rainfall cores, marked by Mentougou

110 (MTG) in Beijing, and Yixian (YX) and Xingtai (XT) in Hebei Province, correspond to the

regions with large topographic gradients (Fig. 1). Please refer to Li et al. (2024) for a detailed analysis of rainfall fine features.
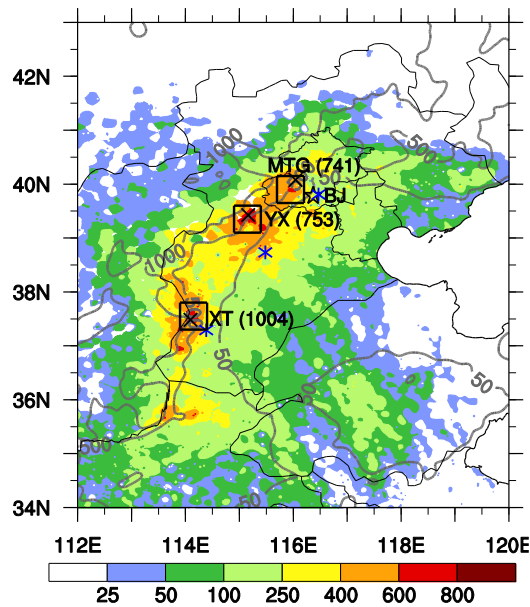
Fig. 1 Spatial distribution of 96-h accumulated rainfall (mm, shadings) from the intensive surface rain gauge observations during the period from 0000 UTC 29 July to 0000 UTC 2 August 2023; Gray contours denote orography from 50 m to 1000 m. Three rainfall cores in Mentougou (MTG) in Beijing, and Yixian (YX) and Xingtai (XT) in Hebei Province are marked by squares, and the values in parentheses indicate the maximum accumulated rainfall (marked by crisscross sign ×) for the regions, respectively. The blue asterisks (＊) represent the locations of wind profiler observational stations near the three rainfall cores. The start (☆) sign indicates the location of Beijing (BJ) City. (Similarly for the rest of figures).

2.2 Wind profiles

The observed wind profiles near MTG, YX, and XT are shown in Fig. 2. Obvious temporal variations in horizontal wind fields can be seen during the rainfall event. Taking the wind profiles near MTG as an example (Fig. 2a), the easterly or southeasterly wind at the levels below 4 km gradually increased from 2 m s^{-1} at 1200 UTC 28 to 24 m s^{-1} at 1200 UTC 30 July 2023. The easterly or southeasterly wind lasted to 0400 UTC 31 July 2023, turned southerly except for near the ground, and then turned southwesterly near 0400 UTC 1 August 2023. After 0400 UTC 31 July, wind speed decreased significantly and then increased drastically. More

138 specifically, the wind speed decreased from 8 m s⁻¹ to 2 m s⁻¹, then increased to 14 m s⁻¹ near 1

139 km above the ground. However, opposite variations can also be seen above 4 km. One can see

140 that the horizontal wind shifted from southwesterly to southerly, then back to southwesterly.

141 Overall, the shift in wind direction and speed altered vertical wind shear, which directly affected

142 the development and organization of subsequent convection (Pucik et al., 2021). Similar

143 variations can also be found at YX and XT stations, although the timing of changes is not

144 synchronized (Fig. 2c,d). The variations proceeded from south to north, starting first at XT and

145 finally at MTG, as the typhoon moved from south to north.

删除的内容：

146
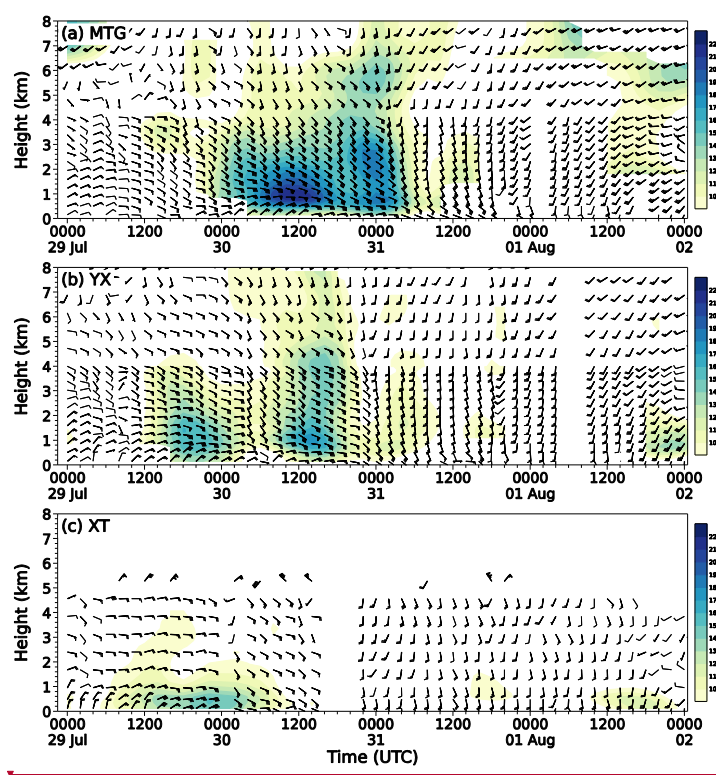
147 **Fig. 2** Temporal evolution of wind profile (a full barb is 4 m s⁻¹, and shadings denote wind

148 speed over 10 m s⁻¹) from observations near (a) MTG, (b) YX, and (c) XT during the period of

149 0000 UTC 29 July to 0000 UTC 2 August 2023. Note only the wind profile below 5 km above

150 the ground can be observed due to the limitation of the instrumentation near Xingtai (XT). (see

151 Fig. 1 their locations).
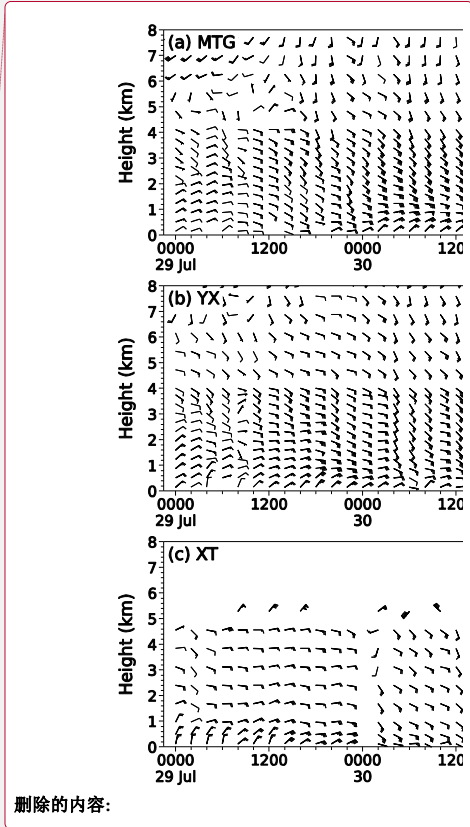
2.3 Synoptic conditions on 28 July 2023

Figure 3 displays a weather chart at 500 hPa at 1200 UTC 28 July 2023. One can see that the large-scale flow patterns exhibited a coexistence of the tropical storm Khanun(2306) with a remnant vortex originating from typhoon Doksuri(2305)*. Note that the Khanun was in the rapid development stage, while the vortex weakened significantly at this time. Another important weather system was the WPSH (denoted by the 588 isoline) with a square-head shape on its western border. Clearly, a water vapor transportation passage was built due to the cyclonic circulation of the tropical storm in combination with the anticyclonic circulation on the southwest of the WPSH. As a result, central and North China was covered by high precipitable water (PW) of over 68 mm. Similar patterns can be viewed at the level of 850 hPa (not shown).
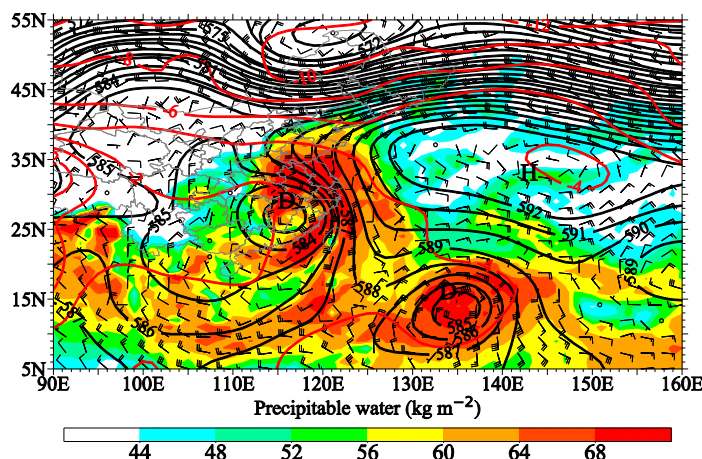
Fig. 3 Weather chart at 500 hPa at 1200 UTC 28 July 2023: Geopotential height (black-contoured at 15 gpm intervals), temperature (red-contoured at 2°C intervals), wind barbs (a full barb is 4 m s^{-1}), and precipitable water (kg m^{-2}, shadings).

3. Model configuration and verification

3.1 Model description

In this study, the persistent heavy rainfall event is reduplicated with the WRF model version 4.1.3. The WRF model is configured in two-way nested grids of horizontal grid sizes of 9 km, 3 km, and 1 km. Figure 4 displays the geographical coverage of the WRF model domains, with the grid points of 901(nx)×601(ny), 973×1231, and 1231×1591 for the outer,

---

*The typhoon Doksuri(2305) weakened to a typhoon remnant vortex as it was passing through East China's Anhui Province. The China Meteorological Administration (CMA) stopped issuing updates on the Doksuri at 0300 UTC 29 July 2023. The remnant of Doksuri remained in a vortex in the lower troposphere, although its wind force diminished as it moved northward.

删除的内容: of a remnant vortex originating from typhoon Doksuri(2305)* and tropical storm Khanun(2306).

删除的内容: The former weakened significantly into a vortex at this time, while the latter was in the rapid development stage

intermediate, and inner domains, respectively. The outermost domain (i.e., D01) is centered at 115°E, 35°N, and a total of 58 sigma levels is assigned in the vertical with the model top fixed at 20 hPa. Since the rainfall is closely related to the spatial distribution of orography over North China (Fig. 1), the Shuttle Radar Topography Mission (SRTM) high-resolution (90 m) topographic data is employed in the present simulation. It should be noted that the model vertical level distribution was carefully tested and has achieved good performance (Yin et al., 2020; Yin et al.,2022a; Yin et al.,2018; Yin et al.,2022b). The WRF model physics schemes are configured with the YSU scheme for the planetary boundary layer (Hong et al., 2006), the revised MM5 Monin-Obukhov (Jimenez) scheme for the surface layer (Jiménez et al., 2012), and the Unified Noah Land Surface Model (Tewari et al.,2004). The rapid radiative transfer model (RRTM) (Mlawer et al.,1997) and the Dudhia scheme (Dudhia,1989) for longwave and shortwave radiative flux calculations, respectively. The Kain-Fritsch cumulus parameterization scheme (Kain,2004) is utilized for the outer two coarse-resolution domains but is bypassed in the finest domain (i.e., D03). The Thompson-ensemble cloud microphysics scheme is applied for explicit cloud processes (Thompson et al.,2008; Yin et al.,2022a).
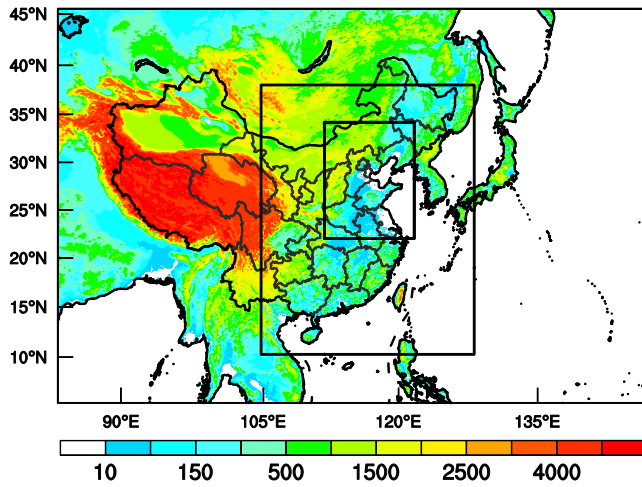
Fig. 4 The WRF model orography (m, shadings) and the nested model domains used for simulations with the grid sizes of 9 km (D01), 3 km (D02), and 1 km (D03).

The WRF model is integrated for 108 hours, starting from 1200 UTC 28 July 2023, with outputs at 6-min intervals. The model outputs in the first 12 h are considered as the spin-up process and thus are not used for the present work. The initial and outermost boundary conditions are interpolated from the final operational global analysis of 1-degree by 1-degree data at 6-h intervals from the Global Forecasting System of the National Centers for

Environment Prediction (NCEP). In order to force large-scale fields consistent with the driving fields, grid analysis nudging is activated by performing the Four-Dimension Data Assimilation (FDDA) throughout the model integration (Bowden et al.,2012; Stauffer et al.,1991). The innermost domain (i.e., D03) outputs are validated and used for further analysis, and the outermost domain (i.e., D01) outputs are used to demonstrate weather-scale dynamical and thermal features. Wind profiler and surface hourly observations are provided by the National Meteorological Information Center (NMIC) of the China Meteorological Administration (CMA) after strict quality control.

3.2 Model verification

Figure 5 shows the spatial distribution of 96-h accumulated rainfall from the simulation during the period from 0000 UTC 29 July to 0000 UTC 02 August 2023. Generally speaking, the WRF model replicates well the spatial distribution of heavy rainfall. The heavy rainfall belt coinciding with the orography with three rainfall cores is reproduced well, and the simulated extreme rainfall amount compares favorably to the observed. Note that the model produces a peak 96-h accumulated rainfall of 778 mm over the XT region, while the maximum rainfall of 1004 mm was observed over the XT region. Despite the simulation underestimates rainfall over this region, it captures the main features of rainfall over central and North China.
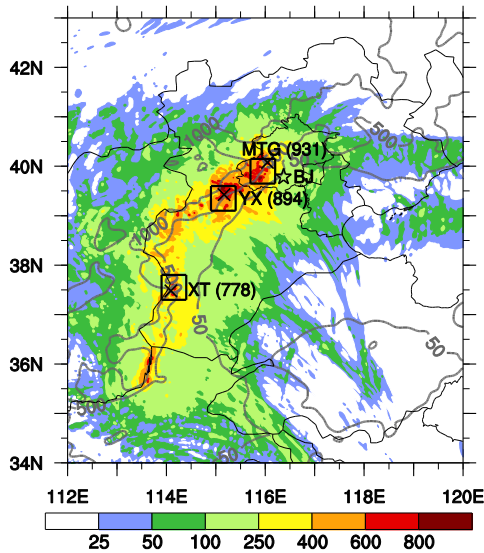
Fig. 5 Same as in Fig. 1 but for the simulated rainfall (mm, shadings).

220   Figure 6 compares the spatial distribution of daily rainfalls between observations and

221   simulations during the period from 0000 UTC 30 July to 0000 UTC 2 August 2023. From

222   observations, one can see that the daily rainfalls show obvious variations. On the first day (Fig.

223   6a), the rainfall occurred mainly in northern Henan and southern Hebei, on the east side of the

224   Taihang Mountains with the rainfall cores over 250 mm. On the next day (Fig. 6b), the rainfall

225   extended significantly northeastward, and a new strong rainfall core occurred, covering central

226   Hebei Province and southwest Beijing. On the third day (Fig. 6c), rainfall was significantly

227   reduced in both coverage and intensity, mainly occurring in Beijing and the surrounding areas.

228   On the fourth day (Fig. 6d), rainfall moved eastward and weakened rapidly. It is apparent that

229   the model reproduces the evolutions of the rainfall (Fig. 6e-h), with general characteristics that

230   are similar to the observed (Fig. 6a-d).

删除的内容: e

删除的内容: h

231

232
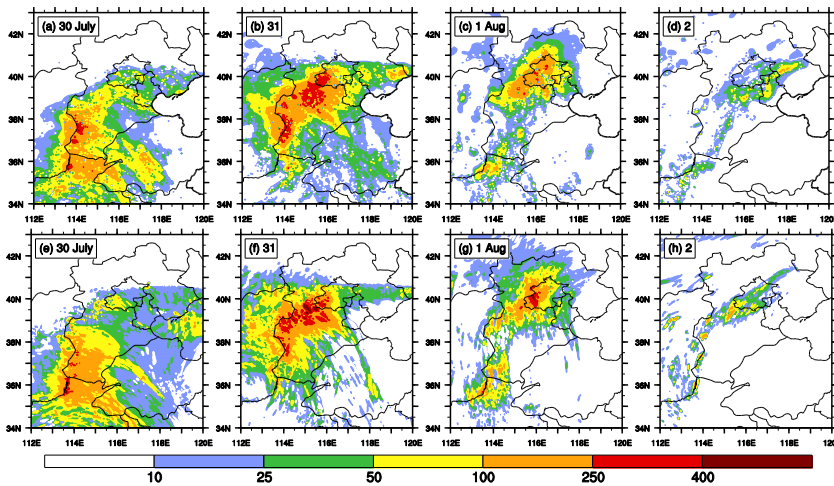
Fig. 6 Spatial distribution of (a-d) observed and (e-h) simulated daily rainfall (mm) during the

234   period from 0000 UTC 30 July to 0000 UTC 2 August 2023.

235   Figure 7 compares the time series of hourly rainfall rates between the observed and

236   simulated over the MTG, YX, and XT regions. The rainfall event is characterized by long

237   duration, widespread coverage, and high accumulation. As has been mentioned above, the

238   rainfall extended from south to north, covering Henan, Hebei, and Beijing. The rainfall first

239   occurred in the XT region and ended near 0000 UTC 31 July 2023. As the rainfall moved

240   northeastward, both the MTG and YX regions occurred, ending nearly at 0000 UTC 2 August.

243 The observed timings of initiating and ending of the rainfall event are well replicated by the

244 WRF model. Besides, the observed peaks are reproduced, although there are some timing errors.

245 For example, the strongest rainfall occurred over the MTG region during the period from 0000

246 UTC to 0600 UTC 31 July. However, the simulated strongest rainfall has a 6-h lag, occurring

247 from nearly 0600 UTC to 1200 UTC 31 July. Overall, good agreements between the simulation

248 and observations are obtained in terms of the timing and location in the spatial distribution of

249 rainfall.

250
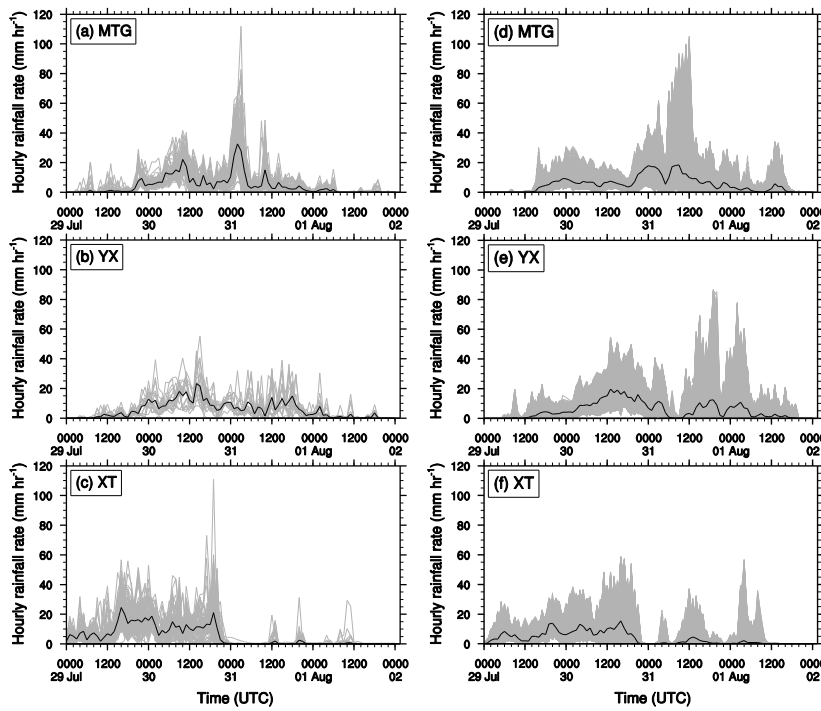
251 **Fig. 7** Time series of (a-c) rain gauge observations and (d-f) simulation hourly rainfall rates

252 (gray lines, mm hr^{-1}) for all stations/grid points over the (a, d) MTG, (b,e) YX, and (c,f) XT

253 regions during the period of 0000 UTC 29 July to 0000 UTC 02 August 2023. The black line

254 denotes the domain-averaged hourly rainfall rates of all stations (grid points) from observations

255 (simulations). (see Fig. 1 their locations). In total, 74, 19, and 67 observations are used for (a)

256 MTG, (b) YX, and (c) XT, respectively. For the simulation, there are (d) 2296, (e) 2365, and (f)

257 2420 grid points.

258 The evolution of the simulated wind profile is presented in Fig. 8. Similar to the observed

259 (Fig. 2), the simulated easterly wind gradually increased from nearly 1200 UTC 29 July,

260 corresponding to the start of the precipitation (Fig. 6e–h). The horizontal wind experienced from

261 easterly to southerly except for near the ground, and then turned to southwesterly with wind

262 speed decreasing significantly. Overall, the variations of the simulated wind profile were

263 consistent with those observed, indicating that the WRF model well captured the main features

264 of the wind profile. Based on the wind profile and rainfall features, the simulated rainfall is

265 roughly divided into two stages. The shift moments (roughly marked by thick black lines) are

266 near at 0800 UTC 31, 2000 UTC 30, and 1600 UTC 30 July for the MTG, YX, and XT regions,

267 respectively. It should be noted that the wind field was significantly influenced by Typhoon

268 Khanun (2306) and the remnant vortex originating from Typhoon Doksuri(2305) in the present

269 event. As the typhoon gradually moved northwestward and the vortex weakened, the first to be

270 affected was Xingtai (XT) in the south, then Yixian (YX) in the center, and finally Mentougou

271 (MTG) in the north. Therefore, the wind shift occurred at different moments.

272
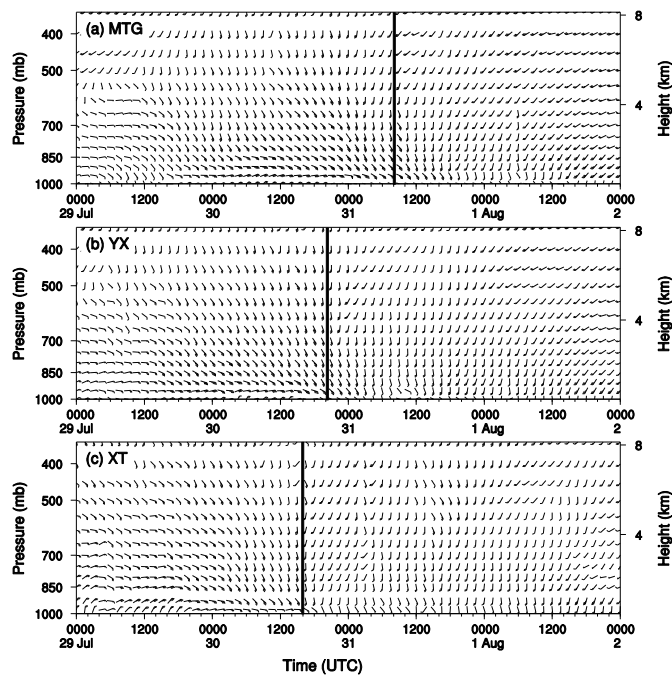
273 **Fig. 8** Same as Fig. 2 but for the simulated. The black lines denote wind shift from southeasterly

274 to southerly/southwesterly over the levels in the low to middle troposphere, which roughly

275 divided the rainfall into two stages.

4. Unique features for the extreme rainfall

4.1 Dominant dynamic processes for convection initialization

The evolution of dynamical and thermal systems of the rainfall event in the first stage is shown in Fig. 9. Although only a remnant vortex remained over central China at this time, typhoon Doksuri had an important influence on the WPSH when it was strong as a super typhoon. Several days before the rainfall event, the super typhoon Doksuri was close to the WPSH, and the southwest WPSH edge was within the typhoon's outer region. Owing to the inflow mass flux entering the typhoon region, and thus the southwest part of WPSH was severely destroyed by typhoon Doksuri (Sun et al.,2015). As a result, the west boundary of the WPSH appeared to an eastward retreat from 500 hPa to 850 hPa, showing an inclined vertical distribution on the western boundary, especially from 700 hPa to 850 hPa. Capped by the inclined WPSH, water vapor was mainly transported to North China through a passage nearly under 850 hPa which is built by the typhoon remnant vortex and the tropical storm Khanun. At 500 hPa (Fig. 9a), the WPSH (represented by the 588 isoline) covered a large part of eastern China, with an unusual westward extension of the northwest corner to northwest China. The northwest corner extended much further westward, compared to that before 12-h (Fig. 3). Similar patterns can be seen at 700 hPa (Fig. 9b), but the west boundary of WPSH (represented by the 316 isoline) retreated to the East China Sea except for the northwest corner. At 850 hPa (Fig. 9c), the WPSH (represented by the 156 isoline) completely retreated to the western Pacific, which was far away from China.

The spatial distribution of the high PW was consistent with that of a large equivalent potential temperature (θ_e) of 344K at 500 hPa, indicating that the 334K contour covered a relatively warm and/or wet region (Fig. 9a). Most important, the boundary of the high PW corresponded to the large value of the potential temperature gradient over 8K on the east side and 12K on both north and west sides. Previous studies (e.g., Rao et al.,2023) proposed that the heavy rainfall region was closely attributed to the distributions of θ_e. Although the warm and moist conditions were favorable for precipitation, the unfavorable large-scale forcings explain well why no deep convection was formed over this region (marked with a dashed-line box in Fig. 9c,d). The convergence, resulting from changes in wind direction and wind speed, was conducive to triggering convection. Consequently, the weak convergence led to weak lifting and consequent precipitation. Since the convergence occurred at the junction of cold and warm

删除的内容: Characteristics of the rainfall event

删除的内容: 7b

air masses, like a warm front rainfall, rainfalls were formed in low intensity but long duration and widespread coverage. It is important to note that the spatial distribution of rainfall is usually considered to be consistent with the western boundary of WPSH (i.e., the 588 isoline) at 500 hPa. However, the spatial distribution of rainfall in the present event is consistent with the dense zone of θ_e, instead of the WPSH. Therefore, in addition to the isoline 588 at 500 hPa, the spatial distribution of θ_e needs to be given more attention in future operational forecasts.
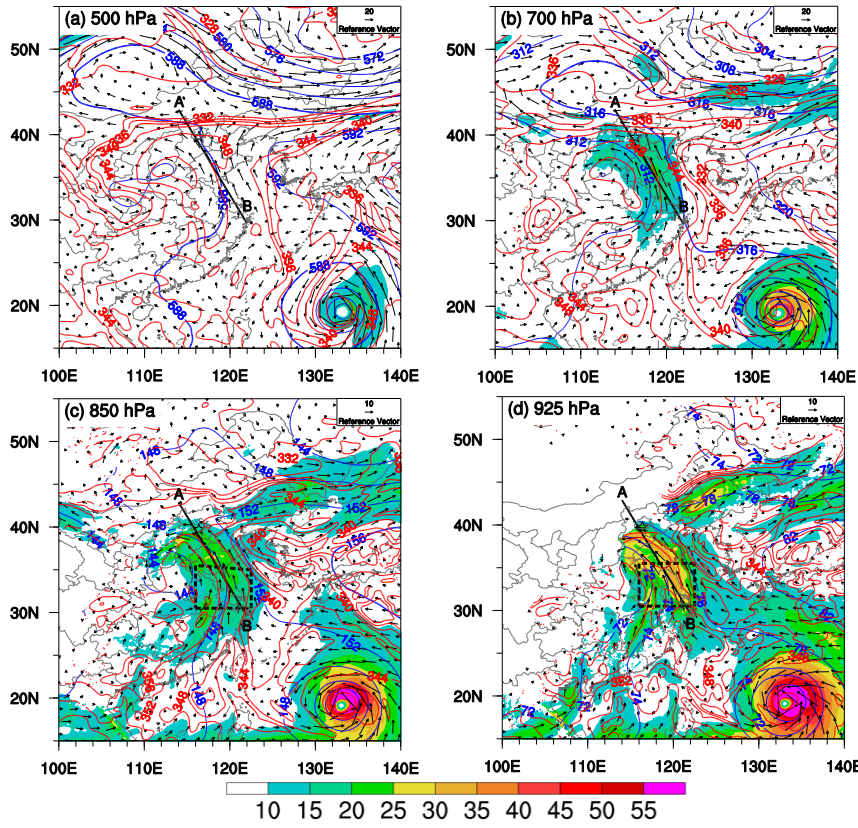
Fig. 9 Spatial distribution of geopotential height (blue contoured at 40 gpm), equivalent potential temperature (red contoured at 2K intervals, θ_e), wind bars (a full barb is 4 m s^{-1}), and water vapor flux (g s^{-1} cm^{-1} hPa^{-1}, shadings) from the model D01 at 0000 UCT 30 July 2023: (a) 500 hPa, (b) 700 hPa, and (c) 850 hPa, and (d) 925 hPa. The isolines of 588, 316, and 156 are bolded to represent the WPSH at 500 hPa, 700 hPa, and 850 hPa, respectively. The convergence zone of southeast and southwest flows is marked by a dashed line box in panels (c) and (d). The thick black line A–B denotes the locations for cross-section along the water vapor transport pathway used in Fig. 10.

325   The warm and moist features over North China can also be seen from the cross-section

326   along the line A–B as shown in Fig. 10. The western orography region was controlled by cold

327   air mass over the levels above 3.0 km. Under the conditions, significant equivalent potential

328   temperature gradients were established between the warm and cold air masses, similar to a

329   warm front. Meanwhile, owing to the blocking of orography below 1.3 km and the strong cold

330   air mass above 3.0 km, only the southeasterly flows between 1.3 and 3.0 km above the sea level

331   can overpass the mountains. It should be noted that although the warm and moist southeasterly

332   flows were lifted by the orography, they could not move further upward to trigger convection

333   because of the local capped cold and dry air masses overhead. Consequently, convergence

334   mainly resulted from the changes in wind direction and wind speed led to upward motion. As

335   the warm and moist air was lifted, condensation occurred and thus generated precipitation. It

336   should be emphasized that the lifting was too weak to allow convection to be highly organized

337   (Fig. 10). For example, the updrafts in strong deep convective systems (e.g., Yin et al.,2020;

338   Yin et al.,2022c) are 5-10 times as large as the updrafts in the present event. Therefore, the weak

339   lifting was responsible for the rainfall in large coverage but low intensity. Besides, the

340   continuous and stable water vapor supply was another favorable factor for the precipitation.

341   Also from Fig. 10, one can see that North China was surrounded by warm dry air masses

342   on the east side and cold dry air masses on both north and west sides. More specifically, the air

343   mass at the levels above 1 km on the east side was over 3°C warmer than surrounding regions,

344   but the water vapor mixing ratio (q_v) was less than 14 g kg^{-1} (humidity was less than 70%)

345   because this region was controlled by the WPSH. The warm-dry cap overhead explains well

346   the absence of convection and rainfall over this region (cf. Figs. 5 and 6). On the north and west

347   sides, the air masses were dry with q_v less than 2 g kg^{-1}. The air was over 3°C colder than the

348   surrounding region except for the air near the ground. Note that warm air near the ground might

349   be associated with radiative heating from the ground. Capped by the cold and dry air overhead

350   explains why convection could not be advanced over the mountains.
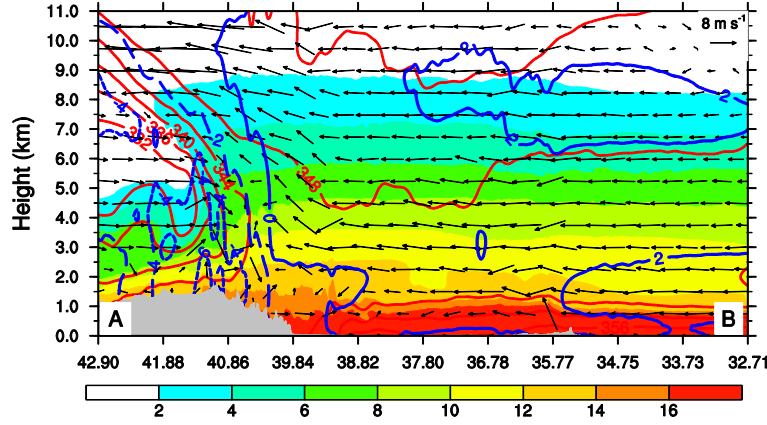
Fig. 10 Vertical cross-section along line A–B given in Fig. 9 of temperature deviations (blue-contoured at 2°C intervals) from their level-averaged values in the cross-section, equivalent potential temperature (red-contoured at 4K intervals), water vapor mixing ratio (q_v, g kg^{-1}, shadings), and in-plane flow vectors (vertical motion amplified by a factor of 20) at 0000 UCT 30 July 2023, respectively. Gray shadings denote terrain.

In the second stage (Fig. 11), obvious differences in dynamical and thermal processes can be viewed, compared to those in the first stage (cf. Fig. 9). At 500 hPa (Fig. 11a), the WPSH further expanded westward with its western border reaching western China. It should be emphasized that the southwest part of WPSH was severely damaged by the rapid intensification of Khanun into a super typhoon. Meanwhile, as the trough deepened over northeastern China, cold air from the north poured southward. Consequently, a north-south orientated θ_e dense zone was established over eastern China. Similar patterns in θ_e and horizontal wind field can be seen at 700 hPa (Fig. 11b). However, the WPSH (represented by the 316 isoline) was further disrupted as the Khanun continued to intensify, appearing that the WPSH retreated to the East China Sea except for the northwest corner. The north-south orientated θ_e dense zone greatly prevented water vapor from transporting to North China above 850 hPa, and thus water vapor was mainly transported to North China by a shallow southeasterly flow near the ground (Fig. 11c,d). Consequently, the water vapor flux was significantly reduced (Fig. 12a). Besides, North China was dominated by southerly flows over levels above 500 hPa, and thus mid-tropospheric wind shear was significantly enhanced.
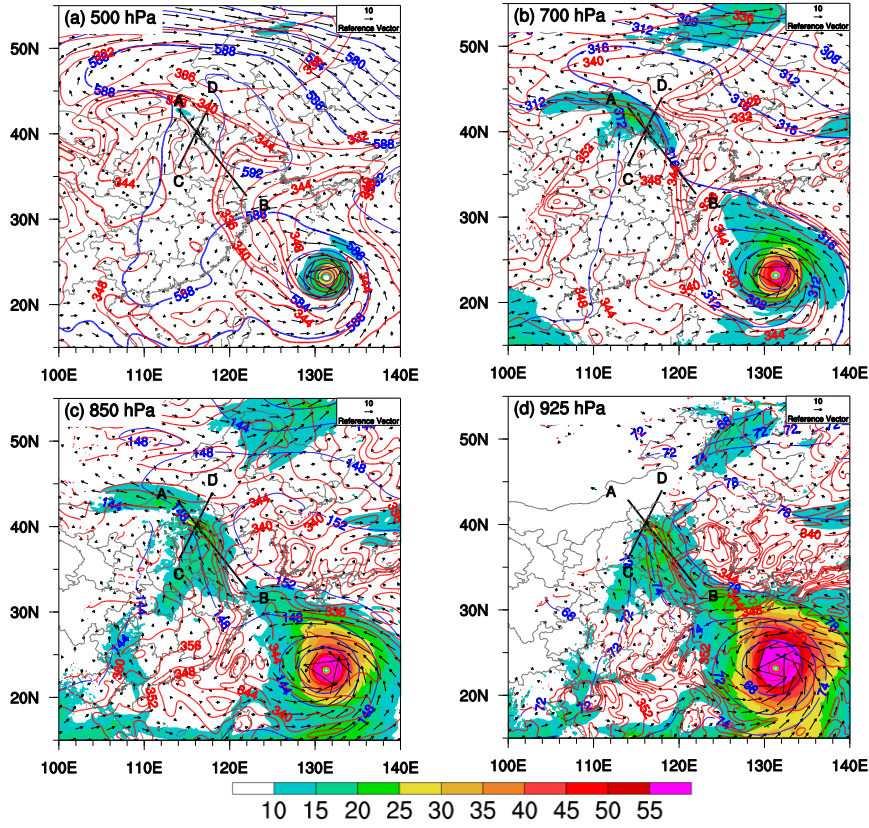
Fig. 11 Same as Fig. 9 but for 0800 UTC 31 July 2023. Thick black lines A–B and C–D denote the locations for the cross-section in Fig. 12.

As addressed above, variations in environmental conditions caused consequent rainfall changes in nature. Especially, the shift in the wind field brought changes in thermodynamic processes and water vapor sources. Before the wind shift (Figs. 9 and 10), water vapor was mainly from the East China Sea associated with the cyclonic circulation of the typhoon remnant vortex and the tropical storm Khanun and southeasterly flow below 925 hPa. After the shift, water vapor flux was significantly reduced from both southwesterly and southeasterly flows (Fig. 11). Under the framework, convections were triggered by orographic blocking and lifting of southerly/southwesterly flows as convective instability air approached orography (Fig. 12). Unlike in the first stage, convections were further developed over mountains northward, forming deep convections (Fig. 12b). One of the reasons is that the cold air on the north side

384 moved northward. Comparatively speaking, the convections in the second stage are much
385 stronger and deeper than those in the first stage. Consequently, the rainfall intensity is increased,
386 compared to those in the first stage (Figs. 7d,e).

387

388
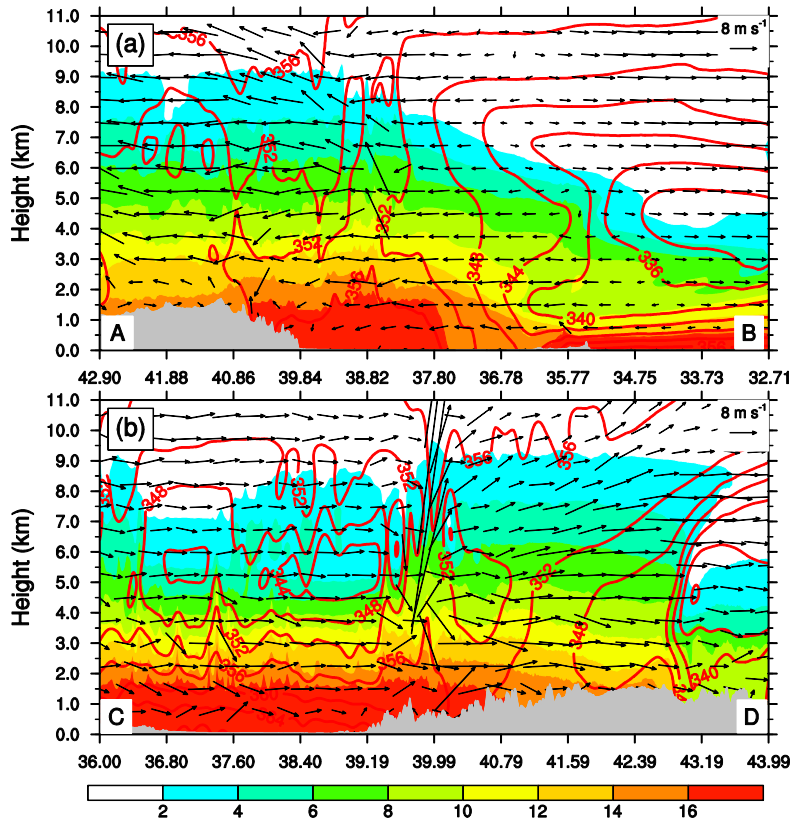
389 **Fig. 12** Vertical cross-sections along lines (a) A–B and (b) C–D given in Fig. 11 of equivalent
390 potential temperature (θ_e, red-contoured at 4K intervals), water vapor mixing ratio (q_v, g kg^{-1},
391 shadings), and in-plane flow vectors (vertical motion amplified by a factor of 10) at 0800 UCT
392 31 July 2023. Gray shadings denote terrain.

393 *4.2 Moisture budget*

394   The shift in wind direction and speed implies a change in water vapor source and rainfall
395 properties (Fig. 13). As stated above, water vapor was mainly from the East China Sea
396 associated with the cyclonic circulation of typhoon Khanun before the wind shift, and was
397 fueled by the southeasterly flow below 925 hPa. After the shift, the water vapor supply was

significantly reduced from both southwesterly and southeasterly flows. Figure 13 shows the time-height cross-sections of moisture flux across eastern, southern, western, and northern boundaries and total lateral boundary moisture flux for the MTG region. The moisture flux is calculated as

$$QFlux = \int_0^L q_v \vec{v} dl .$$

Here, $QFlux$ is moisture flux across one of the four boundaries, and q_v, $\vec{v}$, and L are water vapor mixing ratio, wind vector, and the length of the boundary, respectively. The TOT is a summation of the $QFluxs$ from the four boundaries by taking inward(outward) as positive(negative).

One can see that the MTG region experienced vigorous lower-to-middle level inward (outward) moisture fluxes across their eastern and southern (western and northern) boundaries. For the eastern boundary (Fig. 13a), the inward moisture flux began to increase gradually from 0000 UTC 29 July, with the maximum values over 13,500 kg kg^{-1} m^2 s^{-1} occurring between 1200 UTC 30 and 0000 UTC 31 July 2023. Then, the inward flux moisture decreased rapidly and even transformed to the outward flux at 0000 UTC 1 August 2023. The inward moisture flux was mainly concentrated below 3 km above the sea level because upper levels were capped by the warm dry air masses associated with the WPSH (cf. Figs. 9 and 10). However, owing to weak lifting over, most of the water vapor flowed out through the western boundary (Fig. 13b). Meanwhile, part water vapor was transported in this region from the southern boundary except for the lower levels during 0000 UTC 30 to 0000 UTC 31 July 2023 (Fig. 13d). The outward flow water vapor resulted from the northeasterly around flow due to the blocking of the Yanshan Mountains. Similar patterns can be seen in the northern boundary with almost the same outward water vapor flux (Fig. 13c). The temporal evolution of the water vapor flux across the eastern boundary is consistent with that of rainfall over this region (Figs. 13a and 7d), suggesting that rainfall formation was dominated by the inward of water vapor from the eastern boundary. Overall, the inward net moisture fluxes were concentrated in the lower troposphere between 0.5 km and 1.5 km (Fig. 13e), suggesting that most of the water vapor was consumed at this layer by condensation. Despite the high water vapor flux, the water vapor-rich layer is too thin (nearly

428   1 km) to be favorable for the formation of heavy rainfall. Similar patterns can be found over

429   both YX and XT regions (not shown), although there were temporal and quantitative differences.

430
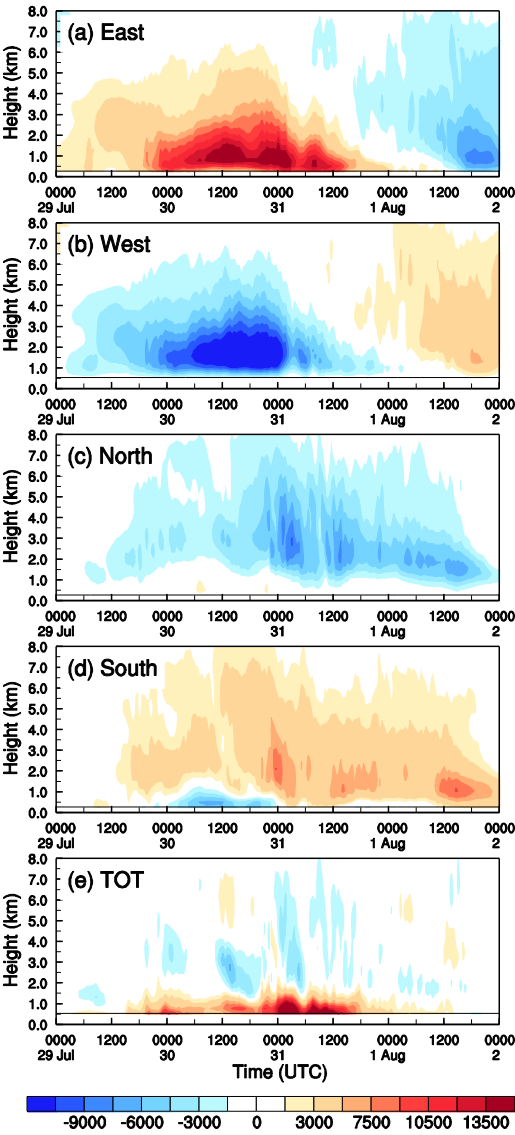
431   **Fig. 13** Time-height cross sections of moisture fluxes (kg kg^{-1} m^2 s^{-1}) through the (a) eastern,

432   (b) western, (c) northern, and (d) southern boundaries of the MTG region in Fig. 1; (e) TOT

433   provides the total net moisture flux of all boundaries.

434   In the second stage, the north-south orientated θ_e dense zone greatly prevented water vapor

from being transported to North China by southeasterly flows from the East China Sea, and thus water vapor was mainly transported to North China across the south boundary (Figs. 13b,d). Unlikely, the water vapor was mainly provided by southeasterly(southwesterly) flow below(above) 500 hPa. Note that the water vapor flux amount was significantly reduced (Fig. 13). Despite the thickening of the water vapor flux layer associated with the southerly/southwesterly flows, the water vapor flux is much less, compared to the first stage. Therefore, the wind shift had strong effects on the reduction in water vapor flux and consequent rainfall over North China. The same results can also be obtained in the YX and XT regions (not shown). It is worth emphasizing that strong hourly rainfalls occurred during the wind shift period (cf. Figs. 2, 7, and 8), suggesting that the changes in wind direction enhanced wind shear and thus promoted the development of convections and consequent precipitation under moisture and instability conditions (Chen et al.,2015; Rotunno et al.,1988; Schumacher and Rasmussen, 2020). Therefore, it is important to pay special attention to environmental wind alterations in future remote rainfall forecasts.

4.3 Properties of convection

Figure 14 shows the temporal evolution of maximum upward motion and radar reflectivity over the MTG region during the rainfall period from 0000 UTC 29 to 0000 UTC 2 August 2023. In the first stage (i.e., before 0800 31 July), most of the maximum updrafts were almost less than 3 m s^{-1}. Owing to the weak updrafts, the storm did not stretch as high as typical convective systems over North China, with hydrometeors concentrated on the levels with a temperature above 0°C (Fig. 14a). As addressed above (Fig. 10), weak updrafts were attributed by the unfavorable large-scale conditions. The vertical distribution of hydrometeor indicates that the warm rain processes were dominant in the persistent rainfall event. The result is consistent with the water vapor consumed layer between 0.5 km and 1.5 km (Fig. 13e). Unlikely, the maximum updraft was over 11 m s^{-1} in the second stage (i.e., after 0800 31 July), which is much stronger than that in the first stage (Fig. 14). Correspondingly, the radar reflectivity penetrated through the 0°C level with a cloud top exceeding 12 km, indicating that both warm and cold rain processes were active in this stage. Correspondingly, the intensity of hourly rainfall increased significantly, with the maximum value exceeding 100 mm (Fig. 7d). Comparatively speaking,

删除的内容: forcings

465 there are larger strong convective areas in the second than those in the first stage. The same
466 features were also found in the regions of YX and XT (not shown). Unlike the usual short-
467 duration heavy rainfall in North China (Mao et al.,2018; Xia and Zhang,2019; Yin et al.,2022b),
468 this precipitation was mainly dominated by warm cloud processes (Fig. 14), consistent with
469 observations (e.g., Fu et al., 2023). As addressed above, the weak updrafts but warm-moist air
470 were responsible for persistent rainfall but low intensity. A detailed analysis of cloud
471 microphysical processes for this event will be given in a forthcoming study, in which all
472 microphysical source and sink terms will be explained.

473
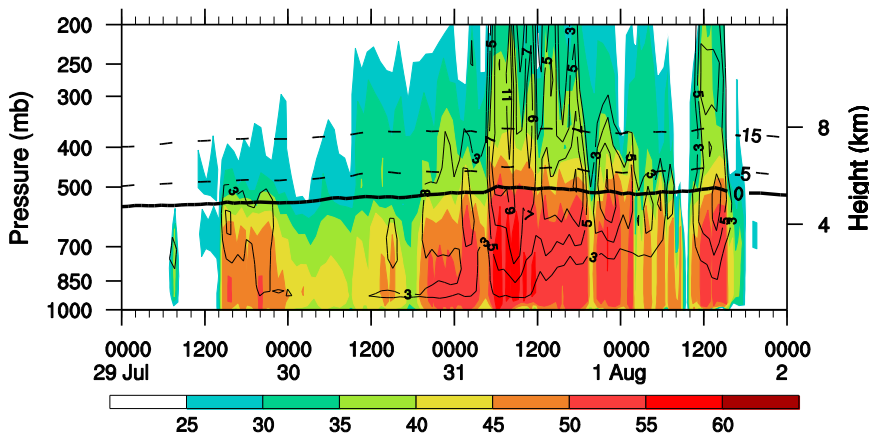
474 **Fig. 14** Time-height cross-section of domain maximum radar reflectivity (dBZ, shadings) and
475 upward motion (contoured at 2 m s^{-1}) taken from MTG region during the period from 0000
476 UTC 29 to 0000 UTC 2 August 2023. The isothermal lines denote the 0°C (the melting layer),
477 -5°C, and -15°C levels, respectively.

478 **5. Conclusions and outlook**

479   In this study, we examined the convective initiation and subsequent persistent heavy
480 rainfall over North China during the period from 29 July to 2 August 2023 with observations
481 and simulations with the WRF model. From observations, the rainfall was featured by long
482 duration and widespread coverage but low intensity, like a warm front rainfall. Firstly, the
483 persistent heavy rainfall event was reproduced by the WRF model. Further analysis based on
484 the simulations shows that this persistent precipitation was caused by a combination of a
485 remnant vortex originating from typhoon Doksuri(2305), the tropical storm Khanun(2306), the

486 west Pacific subtropical high (WPSH) with an unusual westward extension of the northwestern

487 corner, and stable cold dry air from over northern China.

488   According to the simulated wind profiles and rainfall features, the persistent heavy rainfall

489 event was divided into two stages. Figure 15 summarizes the synoptic-scale forcings and

490 possible dynamic mechanisms for the persistent heavy rainfall. In the first stage (Fig. 15a), a

491 water vapor transportation passage was built by a typhoon remnant vortex and a tropical storm

492 Khanun, providing a stable warm moist water vapor supply. Several days before the rainfall

493 event, the southwestern WPSH was within the typhoon Doksuri's outer region, and thus the

494 southwestern WPSH was destroyed by the tropical storm Doksuri. It appears that the west

495 boundary of the western Pacific subtropical high (WPSH) retreated eastward from 500 hPa to

496 850 hPa, showing an inclined vertical distribution on the western boundary, especially from 700

497 hPa to 850 hPa. Capped by the inclined WPSH, water vapor was mainly transported to North

498 China through a water vapor passage under nearly 850 hPa (Fig. 10). Although the warm and

499 moist regions were favorable for precipitation over North China, organized strong convective

500 systems were seldom because of the absence of unfavorable large-scale conditions. At the same

501 time, the orography in the west of North China was controlled by dry cold air mass over levels

502 above 3.0 km. Owing to the blockings of orography below 1.3 km and the strong cold air mass

503 above 3.0 km, only the southeasterly flows between 1.3 and 3.0 km above the sea level can

504 overpass the mountains. Although the warm and moist southeasterly flows were lifted by the

505 orography, they could not go further upward to trigger convections because of the locally

506 capped cold and dry air masses overhead. Under the conditions, significant equivalent potential

507 temperature gradients were established between the warm and cold air masses, similar to a

508 warm front. Consequently, convergence mainly resulted from the changes in wind direction and

509 wind speed led to upward motion. As the warm and moist air was lifted, condensation occurred

510 and thus generated precipitation. However, the lifting was too weak to allow convection to be

511 highly organized (Fig. 14), leading to the rainfall in low intensity but large coverage. Besides,

512 the continuous and stable transportation of water vapor provided by tropical storm Khanun

513 ensured stable precipitation over a long period of over 80 h. Therefore, this event shows similar

514 rainfall features to those of a warm front rainfall with a long duration and widespread coverage

515 but low intensity.

516   In the second stage (Fig. 15b), the WPSH further expanded westward at 500 hPa, with its

517 western border reaching western China. However, the southwest part of WPSH was further

518 damaged by the rapid intensification of Khanun into a super typhoon. Consequently, the

519 embedded warm-dry cover associated with the tilted WPSH was significantly thinned, favoring

520 convective development. Meanwhile, as the trough deepened over northeastern China, cold air

521 from the north poured southward. Consequently, a north-south-orientated equivalent potential

522 temperature (θ_e) dense zone was established over eastern China, which greatly prevented water

523 vapor from being transported to North China (Fig. 12a). However, owing to the clockwise

524 rotated southeasterly flow, a deep southerly (southwesterly) flow was built over North China.

525 Convections were triggered by orographic blocking and lifting of southerly/southwesterly flows

526 as convective instability air approached orography. Unlike the first stage, the convections were

527 further developed over mountains northward, forming deep convections. It should be noted that

528 the northward-moved cold air on the north side was another favorable condition. Therefore, the

529 convections in the second stage are much stronger and deeper than those in the first stage,

530 although water vapor flux is smaller than in the second period. Consequently, the rainfall

531 intensity is increased, compared to that in the first stage. Correspondingly, both warm and cold

532 rain processes were active in the second stage, while warm rain processes were dominant in the

533 first stage.

534

535
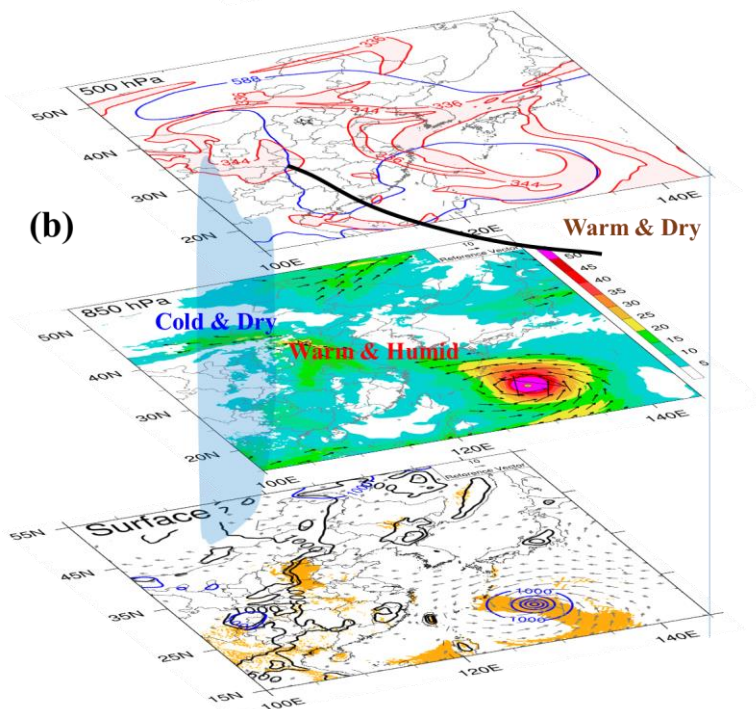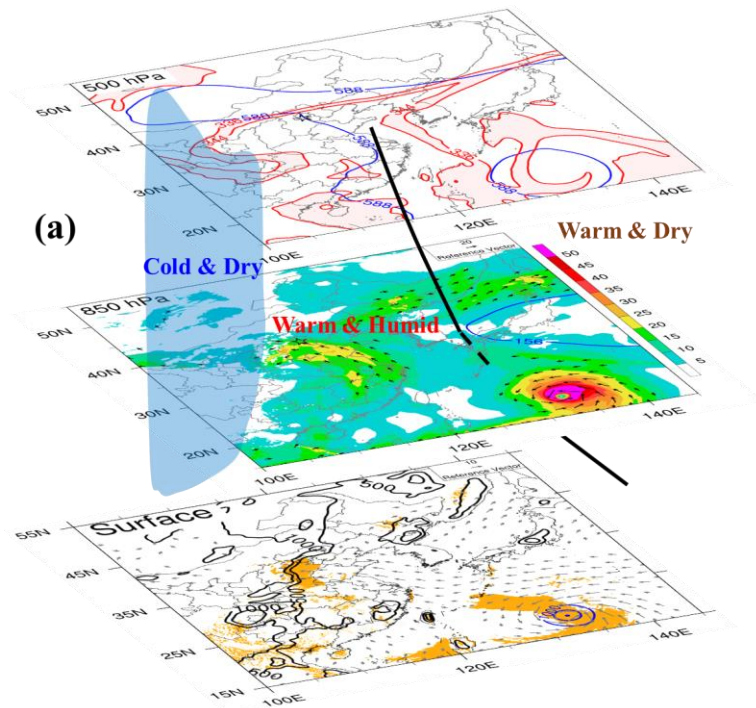
Fig. 15 (a) Three-dimensional diagram of the mechanisms for the persistent heavy in the first stage. Several distinct synoptic systems, including the tropical storm Khanun(2306), a remnant vortex originating from the typhoon Doksuri(2305), quasi-stationary cold dry air masses, and an abnormal western Pacific subtropical high (WPSH) with inclined vertical distribution on the western boundary (thick black line). Blue lines marked with 588 and 156 represent the WPSH at 500 hPa and 850 hPa, respectively. Red lines denote the spatial distribution of equivalent potential temperature (θ_e) dense zone between 336 K and 344K. At 850 hPa, black arrows indicate jets with wind speed over 12 m s^{-1}, and shadings denote water vapor flux. Orange shadings imply 96-h accumulated rainfall over 200 mm; blue contours denote sea level pressure; gray arrows denote surface (i.e., z =10 m) horizontal wind with wind speed over 5 m s^{-1}, and black contours indicate orography (m). (b) Same as (a) but for rainfall in the second stage.

In this study, we have gained principal results of the persistent heavy rainfall event. It is important to note that the spatial distribution of rainfall is usually considered to be consistent with the western boundary of WPSH (i.e., the 588 isoline) at 500 hPa. In the present event, the spatial distribution of rainfall is consistent with the dense zone of θ_e, rather than the western boundary of WPSH. Therefore, in addition to the 588 isoline, the spatial distribution of θ_e needs to be given more attention in future operational forecasts. Besides, we should give weight to environmental wind shifts, which may lead to changes in convections and the nature of consequent precipitation. Although reasonable dynamic mechanisms for the present persistent heavy rainfall have been proposed, there are still several questions that need to be answered. Among those, more work is required to understand detailed cloud and precipitation processes. In addition, diagnostic and budget analyses will be conducted to understand how the orography facilitates the generation of the rainfall belt with three rainfall cores along the mountains. Nevertheless, the concept of synoptic-forcing-based forecasting is discussed as it might apply to a broader spectrum of forecast events than just over North China.

Code and data availability

The source code of the Weather Research and Forecasting model (WRF v4.1.3) is available at https://github.com/wrf-model/WRF/releases (last access 1 August 2024). The National Centers

for Environmental Prediction (NCEP) Global Forecast System one-degree final analysis data at 6 h intervals used for the initial and boundary conditions for the specific analyzed period can be downloaded at https://rda.ucar.edu/datasets/d083002/ (last access 1 August 2024). Modified WRF model codes and all the data used in this study are available from the authors upon request.

Author contributions

Conceptualization: JY, JS, and XL; methodology: JY and JS; data curation: JY and FL; writing – original draft preparation: JY, and FL; writing – review and editing: JY, ML, RX, XB, and JS; project administration: XL; funding acquisition: JY and XL. All authors have read and agreed to the published version of the paper.

Competing interests

The contact author has declared that none of the authors has any competing interests.

Acknowledgments

The authors acknowledge the use of the NCAR Command Language (NCL) in the preparation of figures.

Financial support

This study is jointly supported by the National Key R&D Program of China (2022YFC3003903), National Natural Science Foundation of China (42075083), Open Project Fund of China Meteorological Administration Basin Heavy Rainfall Key Laboratory (2023BHR-Z03), and the Development Foundation of Chinese Academy of Meteorological Sciences (2019KJ026).

References

Bao, X., Sun, J., Yin, J., Gao, X., Li, F., Liang, X., Gu, H., Xia, R., Li, M., Wu, C., and Feng, J.: What Caused the Differences between "23·7" and "96·8" Extreme Rainfall Events in North China under a Similar Synoptic Background?, Journal of Meteorological Research, 88, 1-19, https://doi.org/10.1007/s13351-024-3192-0, 2024.

Bowden, J. H., Otte, T. L., Nolte, C. G., and Otte, M. J.: Examining Interior Grid Nudging Techniques Using Two-Way Nesting in the WRF Model for Regional Climate Modeling, J. Clim., 25, 2805-2823, https://doi.org/10.1175/JCLI-D-11-00167.1, 2012.

Chen, Q., Fan, J., Hagos, S., Gustafson Jr, W. I., and Berg, L. K.: Roles of wind shear at different vertical levels: Cloud system organization and properties, Journal of Geophysical Research: Atmospheres, 120, 6551-6574, https://doi.org/10.1002/2015JD023253, 2015.

Ding, Y.: A case study on the excessively severe rainstrom in Honan province, early in August, 1975, Scientia Atmospherica Sinica, 2, 276-289. (in Chinese), 1978.

Dudhia, J.: Numerical Study of Convection Observed during the Winter Monsoon Experiment Using a Mesoscale Two-Dimensional Model, Journal of the Atmospheric Sciences, 46, 3077-3107, https://doi.org/10.1175/1520-0469(1989)046<3077:NSOCOD>2.0.CO;2, 1989.

Feng, W. and Cheng, L.: Nonhydrostatic numerical simulation for the "96.8" extraordinary rainstorm and the developing structure of mesoscale system, 16, 423-440, 2002.

Fowler, H. J., Blenkinsop, S., Green, A., and Davies, P. A.: Precipitation extremes in 2023, Nature Reviews Earth & Environment, 5, 250-252, https://doi.org/10.1038/s43017-024-00547-9, 2024.

Fu, J., Quan, W., Mai, Z., Luo, Q., Chen, T., Li, X., Xu, X., Zhu, W., Hua, S., and Han, X.: Preliminary study on the refined characteristics of rainfall intensity and dynamic and thermodynamic conditions in the July 2023 severe torrential rain in north China, Meteorological Monthly, 49, 1435-1450, 10.7519/j.issn.1000-0526.2023.112701, 2023. (In Chinese with English abstract)

带格式的: 字体: (默认) Times New Roman, 小四

619   Gao, Z., Zhang, J., Yu, M., Liu, Z., Yin, R., Zhou, S., Zong, L., Ning, G., Xu, X., Guo, Y.,

620   Wei, H., and Yang, Y.: Role of Water Vapor Modulation From Multiple Pathways in the

621   Occurrence of a Record-Breaking Heavy Rainfall Event in China in 2021, Earth and

622   Space Science, 9, e2022EA002357, https://doi.org/10.1029/2022EA002357, 2022.

623   Hirata, H. and Kawamura, R.: Scale interaction between typhoons and the North Pacific

624   subtropical high and associated remote effects during the Baiu/Meiyu season, Journal of

625   Geophysical Research: Atmospheres, 119, 5157-5170,

626   https://doi.org/10.1002/2013JD021430, 2014.

627   Hong, S.-Y., Dudhia, J., and Chen, S.-H.: A Revised Approach to Ice Microphysical

628   Processes for the Bulk Parameterization of Clouds and Precipitation, Monthly Weather

629   Review, 132, 103-120, https://doi.org/10.1175/1520-

630   0493(2004)132<0103:ARATIM>2.0.CO;2, 2004.

631   Hu, G., Lu, M.-H., Reynolds, D., Wang, H.-K., Chen, X., Liu, W.-C., Zhu, F., Wu, X.-W., Xia,

632   F., Xie, M.-C., Cheng, X.-N., Lim, K.-S., Zhai, B.-P., and Chapman, J.: Long-term

633   seasonal forecasting of a major migrant insect pest: the brown planthopper in the Lower

634   Yangtze River Valley, J. Pest Sci., 92, https://doi.org/10.1007/s10340-018-1022-9, 2019.

635   Janjić, Z. I.: The step-mountain eta coordinate model: further developments of the convection,

636   viscous sublayer, and turbulence closure schemes, Monthly Weather Review, 122, 927-

637   945, https://doi.org/10.1175/1520-0493(1994)122<0927:TSMECM>2.0.CO;2, 1994.

638   Janjić, Z. I.: Nonsingular implementation of the Mellor-Yamada Level 2.5 Scheme in the

639   NCEP Meso model. NCEP Office Note No. 437, 61 pp., 2002.

640   Jiménez, P. A., Dudhia, J., González-Rouco, J. F., Navarro, J., Montávez, J. P., and García-

641   Bustamante, E.: A Revised Scheme for the WRF Surface Layer Formulation, Monthly

642   Weather Review, 140, 898-918, https://doi.org/10.1175/MWR-D-11-00056.1, 2012.

643   Kain, J. S.: The Kain–Fritsch Convective Parameterization: An Update, Journal of Applied

644   Meteorology, 43, 170-181, https://doi.org/10.1175/1520-

645   0450(2004)043<0170:TKCPAU>2.0.CO;2, 2004.

646   Li, M., Sun, J., Li, F., Wu, C., Xia, R., Bao, X., Yin, J., and Liang, X.: The Fine Precipitation

647   Characteristics of an extreme rainfall event over North China during 29 July to 1 August

648   2023, Journal of Meteorological Research (Submitted), 2023.

649 Lin, Y.-H. and Wu, C.-C.: Remote Rainfall of Typhoon Khanun (2017): Monsoon Mode and

650   Topographic Mode, Monthly Weather Review, 149, 733-752,

651   https://doi.org/10.1175/MWR-D-20-0037.1, 2021.

652 Mao, J., Ping, F., Yin, L., and Qiu, X.: A Study of Cloud Microphysical Processes Associated

653   With Torrential Rainfall Event Over Beijing, Journal of Geophysical Research:

654   Atmospheres, 123, 8768-8791, https://doi.org/10.1029/2018JD028490, 2018.

655 Meng, Z., Zhang, F., Luo, D., Tan, Z., Fang, J., Sun, J., Shen, X., Zhang, Y., Wang, S., Han,

656   W., Zhao, K., Zhu, L., Hu, Y., Xue, H., Ma, Y., Zhang, L., Nie, J., Zhou, R., Li, S., Liu,

657   H., and Zhu, Y.: Review of Chinese atmospheric science research over the past 70 years:

658   Synoptic meteorology, Science China Earth Sciences, 62, 1946-1991,

659   https://doi.org/10.1007/s11430-019-9534-6, 2019.

660 Mlawer, E. J., Taubman, S. J., Brown, P. D., Iacono, M. J., and Clough, S. A.: Radiative

661   transfer for inhomogeneous atmospheres: RRTM, a validated correlated-k model for the

662   longwave, Journal of Geophysical Research: Atmospheres, 102, 16663-16682,

663   https://doi.org/10.1029/97JD00237, 1997.

664 Tomas, P., Pieter, G., and Ivan, T.: Vertical wind shear and convective storms,

665   https://doi.org/10.21957/z0b3t5mrv,   2021.

666 Rao, C., Chen, G., and Ran, L.: Effects of Typhoon In-Fa (2021) and the Western Pacific

667   Subtropical High on an Extreme Heavy Rainfall Event in Central China, Journal of

668   Geophysical Research: Atmospheres, 128, e2022JD037924,

669   https://doi.org/10.1029/2022JD037924, 2023.

670 Rotunno, R., Klemp, J., and Weisman, M.: A Theory for Strong, Long-Lived Squall Lines,

671   Journal of The Atmospheric Sciences - J ATMOS SCI, 45, 463-485,

672   https://doi.org/10.1175/1520-0469(1988)045<0463:ATFSLL>2.0.CO;2, 1988.

673 Schumacher, R. S. and Rasmussen, K. L.: The formation, character and changing nature of

674   mesoscale convective systems, Nature Reviews Earth & Environment, 1, 300-314,

675   10.1038/s43017-020-0057-7, 2020.

676   Stauffer, D. R., Seaman, N. L., and Binkowski, F. S.: Use of Four-Dimensional Data

677   Assimilation in a Limited-Area Mesoscale Model Part II: Effects of Data Assimilation

678   within the Planetary Boundary Layer, Monthly Weather Review, 119, 734-754,

679   https://doi.org/10.1175/1520-0493(1991)119<0734:UOFDDA>2.0.CO;2, 1991.

680   Sun, J., Qi, L., and Zhao, S.: A study on mesoscale convective systems of the severe heavy

681   rainfall in north China by "9608" typhoon, Acta Meteorologica Sinica, 64, 57-71,

682   10.11676/qxxb2006.006, 2006.

683   Sun, Y., Zhong, Z., Yi, L., Li, T., Chen, M., Wan, H., Wang, Y., and Zhong, K.: Dependence of

684   the relationship between the tropical cyclone track and western Pacific subtropical high

685   intensity on initial storm size: A numerical investigation, Journal of Geophysical

686   Research: Atmospheres, 120, 11,451-411,467, https://doi.org/10.1002/2015JD023716,

687   2015.

688   Tewari, M., Chen, F., Wang, W., Dudhia, J., LeMone, M. A., Mitchell, K., Ek, M., Gayno, G.,

689   Wegiel, J., and Cuenca, R. H.: Implementation and verification of the unified NOAH

690   land surface model in the WRF model. 20th conference on weather analysis and

691   forecasting/16th conference on numerical weather prediction, pp. 11-15., 2004.

692   Thompson, G., Field, P. R., Rasmussen, R. M., and Hall, W. D.: Explicit Forecasts of Winter

693   Precipitation Using an Improved Bulk Microphysics Scheme. Part II: Implementation of

694   a New Snow Parameterization, Monthly Weather Review, 136, 5095-5115,

695   https://doi.org/10.1175/2008MWR2387.1, 2008.

696   Wang, Y., Wang, Y., and Fudeyasu, H.: The Role of Typhoon Songda (2004) in Producing

697   Distantly Located Heavy Rainfall in Japan, Monthly Weather Review, 137, 3699-3716,

698   https://doi.org/10.1175/2009MWR2933.1, 2009.

699   Xia, R. and Zhang, D.-L.: An Observational Analysis of Three Extreme Rainfall Episodes of

700   19–20 July 2016 along the Taihang Mountains in North China, Monthly Weather

701   Review, 147, 4199-4220, https://doi.org/10.1175/MWR-D-18-0402.1, 2019.

702   Xu, H. and Li, X.: Torrential rainfall processes associated with a landfall of Typhoon Fitow

(2013): A three-dimensional WRF modeling study, Journal of Geophysical Research: Atmospheres, 122, 6004-6024, https://doi.org/10.1002/2016JD026395, 2017.

Xu, H., Zhang, D., and Li, X.: The Impacts of Microphysics and Terminal Velocities of Graupel/Hail on the Rainfall of Typhoon Fitow (2013) as Seen From the WRF Model Simulations With Several Microphysics Schemes, Journal of Geophysical Research: Atmospheres, 126, e2020JD033940, https://doi.org/10.1029/2020JD033940, 2021.

Xu, H., Li, X., Yin, J., and Zhang, D.: Predecessor Rain Events in the Yangtze River Delta Region Associated with South China Sea and Northwest Pacific Ocean (SCS-WNPO) Tropical Cyclones, Advances in Atmospheric Sciences, 40, 1021-1042, https://doi.org/10.1007/s00376-022-2069-3, 2023a.

Xu, H., Zhao, D., Yin, J., Duan, Y., Gao, W., Li, Y., and Zhou, L.: Indirect Effects of Binary Typhoons on an Extreme Rainfall Event in Henan Province, China From 19 to 21 July 2021. 3. Sensitivities to Microphysics Schemes, Journal of Geophysical Research: Atmospheres, 128, e2022JD037936, https://doi.org/10.1029/2022JD037936, 2023b.

Yang, L., Liu, M., Smith, J. A., and Tian, F.: Typhoon Nina and the August 1975 Flood over Central China, Journal of Hydrometeorology, 18, 451-472, https://doi.org/10.1175/JHM-D-16-0152.1, 2017.

Yin, J., Liang, X., Wang, H., and Xue, H.: Representation of the autoconversion from cloud to rain using a weighted ensemble approach: a case study using WRF v4.1.3, Geosci. Model Dev., 15, 771-786, https://doi.org/10.5194/gmd-15-771-2022, 2022a.

Yin, J., Zhang, D.-L., Luo, Y., and Ma, R.: On the Extreme Rainfall Event of 7 May 2017 Over the Coastal City of Guangzhou. Part I: Impacts of Urbanization and Orography, Monthly Weather Review, 148, 955-979, https://doi.org/10.1175/MWR-D-19-0212.1, 2020.

Yin, J., Gu, H., Yu, M., Bao, X., Xie, Y., and Liang, X.: Synergetic Roles of Dynamic and Cloud Microphysical Processes in Extreme Short-Term Rainfall: A Case Study, Quarterly Journal of the Royal Meteorological Society, 148, 3660- 3676, https://doi.org/10.1002/qj.4380, 2022b.

731 Yin, J., Wang, D., Liang, Z., Liu, C., Zhai, G., and Wang, H.: Numerical Study of the Role of

732 Microphysical Latent Heating and Surface Heat Fluxes in a Severe Precipitation Event in

733 the Warm Sector over Southern China, Asia-Pacific Journal of Atmospheric Sciences, 54,

734 77-90, https://doi.org/10.1007/s13143-017-0061-0, 2018.

735 Yin, J., Gu, H., Liang, X., Yu, M., Sun, J., Xie, Y., Li, F., and Wu, C.: A Possible Dynamic

736 Mechanism for Rapid Production of the Extreme Hourly Rainfall in Zhengzhou City on

737 20 July 2021, Journal of Meteorological Research, 36, 6-25,

738 https://doi.org/10.1007/s13351-022-1166-7, 2022c.